JOURNAL OF COMPUTATIONAL PHYSICS **46**, 309–327 (1982)

# A Monte-Carlo Model of Neutral-Particle Transport in Diverted Plasmas

D. HEIFETZ, D. POST, M. PETRAVIC,
J. WEISHEIT, AND G. BATEMAN*

*Plasma Physics Laboratory, Princeton University,
Princeton, New Jersey 08544*

Received November 13, 1981; revised February 10, 1982

The transport of neutral atoms and molecules in the edge and divertor regions of fusion experiments has been calculated using Monte-Carlo techniques. The deuterium, tritium, and helium atoms are produced by recombination at the walls. The relevant collision processes of charge exchange, ionization, and dissociation between the neutrals and the flowing plasma electrons and ions are included, along with wall-reflection models. General two-dimensional wall and plasma geometries are treated in a flexible manner so that varied configurations can be easily studied. The algorithm uses a pseudocollision method. Splitting with Russian roulette, suppression of absorption, and efficient scoring techniques are used to reduce the variance. The resulting code is sufficiently fast and compact to be incorporated into iterative treatments of plasma dynamics requiring numerous neutral profiles. The calculation yields the neutral gas densities, pressures, fluxes, ionization rates, momentum-transfer rates, energy-transfer rates, and wall-sputtering rates. Applications have included modeling of proposed INTOR/FED poloidal divertor designs and other experimental devices.

## I. INTRODUCTION

A key problem in the design of reactor-sized fusion experiments is the control of particle and heat exhaust. The helium ash produced by the fusion reaction $D + T \rightarrow He_4 + n$ must be removed for long-pulse reactor operation. The helium removal technique, however, must minimize the pumping of tritium. Thermal heat exhaust must be achieved without introducing impurities into the main plasma. Poloidal divertors and pump limiters have been proposed to solve these problems [1].

The performance of divertors and pump limiters depends crucially on the transport of the neutrals created in the device. For example, a design study [1] for the INTOR tokamak uses a single null poloidal divertor (Fig. 1a), shaping the magnetic field so that the plasma at the edge flows into a divertor chamber (dashed region in Fig. 1a). In the divertor chamber (Figs. 1b and 2a), the plasma flows along the field lines until it reaches the neutralizer plate, where an electrostatic sheath forms to keep the ion and electron currents equal. The ions are accelerated across the sheath and recombine

---

* Permanent address: Georgia Institute of Technology, Atlanta, Ga.

0021-9991/82/050309–19$02.00/0

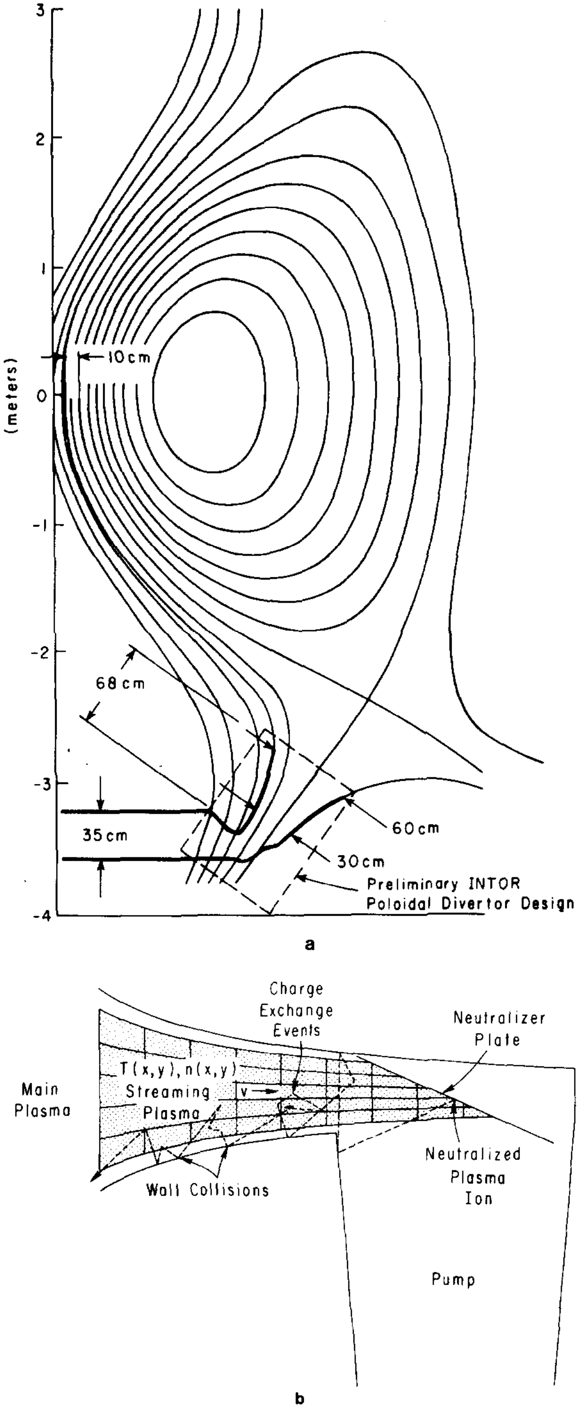

FIG. 1. (a) Poloidal cross section of proposed INTOR Poloidal Divertor configuration. The region enclosed by dashed boundary is also pictured in Fig. 2a. (b) Schematic of the INTOR divertor operation.

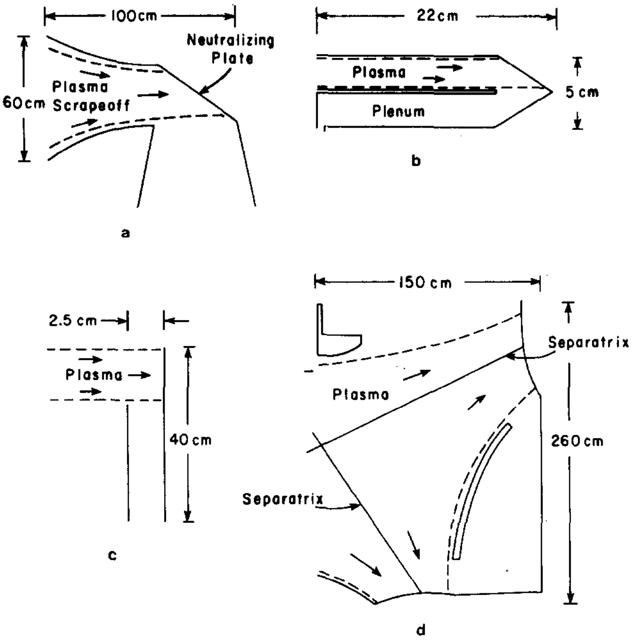

FIG. 2. Cross sections of some geometries modeled. (a) Preliminary INTOR Poloidal Diverter design [1]; (b) PDX scoop [R. Jacobsen, *J. Nucl. Fusion* **22** (1982), 277]; (c) UCLA probe experiment [S. Talmadge and R. Taylor, *Bull. Amer. Phys. Soc.* **26** (1981), 1059]; (d) INTOR/FED design proposal [1].

to form neutrals at the plate. The neutrals then travel down the divertor and the pump, transporting mass, momentum, and energy as they collide with the plasma and walls.

In this paper, we describe an algorithm developed to model this transport using Monte-Carlo techniques, which is flexible enough to be applied to a wide range of divertor problems. For a given particle and energy flux profile, and geometry, we compute (1) the conductances for hydrogen and helium down pumping channels or against the instreaming plasma, and the relative pumping efficiencies for hydrogen and helium, (2) the power loads and erosion rates at the chamber walls, and (3) the ionization and charge-exchange particle, momentum- and energy-exchange rates in the plasma, and the neutral densities and pressures in the exhaust channel. We also note that the techniques developed here are directly applicable to a wide range of questions outside of tokamak modeling.

In Section II the physical models used in the treatment of plasma profile and wall configurations, neutral-plasma reactions, and neutral-wall interactions are presented. In Section III we discuss the Monte-Carlo algorithm. The overall approach is a standard one, and we note only these aspects unique to our problem. In particular, the pseudocollisional method of tracking test flights is described. Test flights deposit scorings of ionizations and charge exchanges at each pseudocollision from which neutral temperatures and densities are derived. A subalgorithm efficiently models wall reflections using Monte-Carlo data from the MARLOWE code [2]. Suppression of test-flight absorption and partial vectorization of the computer code economize code operation. Finally, in Section IV example calculations for a vacuum case and for a proposed INTOR divertor design are given.

Callen *et al.* [3] review our modeling results for advanced divertor design, as well as presenting a detailed comparison with the calculations of Seki *et al.* [4]. The code has been incorporated also into a self-consistent fluid model of divertor plasmas [5].

## II. THE PHYSICAL MODEL

A basic assumption is that plasma conditions remain constant throughout the Monte-Carlo test flights. For experiments in equilibrium for > 100 msec, a time-independent approach is then valid. When the time scale of change is a few tens of microseconds, however, a time-dependent approach is necessary. We describe here only the time-independent model. This model could be modified easily into a time-dependent one by timing the test flights.

### A. *Geometric and Plasma Parameters*

Plasma zone boundaries and chamber walls vary two-dimensionally in the $xy$ plane, and are assumed to be independent of $z$. They are described by piecewise linear approximations. A representative sample of configurations which have been used is shown in Fig. 2.

The plasma density, temperature, and flow velocity direction are specified individually for each zone before the calculation. Plasma flow speed is set at a fixed fraction of

$$((\bar{T}_i + T_e)\bar{m}_i)^{1/2},$$

where $\bar{T}_i$ is the average ion temperature and $\bar{m}_i$ the average ion mass. The plasma flux on the walls, with the appropriate particle reflection and sheath models, provides the source flux boundary conditions for the neutral transport calculation.

### B. *Neutral-Plasma Reactions*

The collision processes considered most important to our calculations and included in it are listed in Table I. The cross sections for reactions (1) and (6)–(8) in Table I are computed from numerical fits in Freeman and Jones [6] and Jones [7], and are used to compute tables of $\langle \sigma v \rangle$ as a function of neutral energy $E_0$ and plasma ion temperature $T_i$, using Gauss–Hermite quadrature. We compute $\langle \sigma v \rangle$ for reactions (2)–(5) and (9) in Table I directly from fits in [6] and [7].

TABLE I

Neutral-Plasma Reactions Included in Our Model[a]

| | | |
|---|---|---|
| (1) | $H^0 + H^+$ | $\rightarrow H^+ + H^0$ |
| (2) | $e + H^0$ | $\rightarrow H^+ + 2e$ |
| (3) | $e + H_2^0$ | $\rightarrow 2H^0 + e$ |
| (4) | $e + H_2^0$ | $\rightarrow H^0 + H^+ + 2e$ |
| (5) | $e + H_2^0$ | $\rightarrow H_2^+ + 2e$ |
| (5a) | $e + H_2^+$ | $\rightarrow 2H^0$ |
| (5b) | $e + H_2^+$ | $\rightarrow H^0 + H^+ + e$ |
| (6) | $He^0 + He^+$ | $\rightarrow He^+ + He^0$ |
| (7) | $He^0 + He^{++}$ | $\rightarrow He^{2+} + He^0$ |
| (8) | $He^0 + H^+$ | $\rightarrow He^+ + H^0$ |
| (9) | $e + He^0$ | $\rightarrow He^+ + 2e$ |

[a] H is hydrogen, deuterium, or tritium. We assume that if $H_2^0$ is ionized in reaction (5), then the $H_2^+$ produced is dissociated instantaneously by reaction (5a) or (5b).

### C. *Wall-Reflection Models*

Two models for reflecting neutral atoms and ions from the divertor walls are included. The first is similar to that of Seki [4] for iron: if $\theta$ is the incident polar angle and $E_{\text{in}}$ the incident energy in electronvolts, the reflection coefficient is

$$\begin{aligned} R_N &= -0.237 \ln(E_{\text{in}}/C) + 0.19, \qquad && \theta \leqslant 40^\circ \\ &= 1, && \theta > 40^\circ, \end{aligned}$$

with $C = 2990.$, $2990.$, and $6290.$ for D°, T°, and He°, respectively. The reflected velocity cosines ($V_x(\text{out})$, $V_y(\text{out})$, $V_z(\text{out})$) vary from specular for $\theta \approx 90^\circ$, to a cosine distribution in polar angle for $\theta \approx 0^\circ$. We use the formulas

$$\begin{aligned} V_x(\text{out}) &= [\cos\theta \sin\alpha + \sin\theta \cos\phi \cos\alpha] \cos\zeta - \sin\theta \sin\phi \sin\zeta, \\ V_y(\text{out}) &= [\cos\theta \sin\alpha + \sin\theta \cos\phi \cos\alpha] \sin\zeta + \sin\theta \sin\phi \cos\zeta, \\ V_z(\text{out}) &= \cos\theta \cos\alpha - \sin\theta \cos\phi \sin\alpha, \end{aligned}$$

where

$$\begin{aligned} \cos\alpha &= -V_z(\text{in}), \\ \cos\zeta &= V_x(\text{in})/(V_x(\text{in})^2 + V_y(\text{in})^2)^{1/2}, \\ \sin\theta &= \cos\alpha \sqrt{\xi}, \end{aligned}$$

and

$$\phi = 2\pi\eta,$$

$\xi, \eta$ being uniform random numbers between 0 and 1. The energy of the reflected neutral is taken to be

$$\begin{aligned} E(\text{out}) &= E_{\text{in}}(-0.22 \ln[E(\text{in})/C] + 0.06)/R_N, && \theta \leqslant 40^\circ \\ &= 0.9E_{\text{in}}, && \theta > 40^\circ. \end{aligned}$$

Hydrogen and helium not reflected are assumed to desorb eventually (in steady state) as molecules or atoms, monoenergetically at the wall temperature, and with a cosine distribution in polar angle. Molecules striking the wall do so at low velocity and are assumed to desorb immediately, with the same cosine distribution assumed for desorbed H and He atoms.

For our second model we use data from the Monte-Carlo code MARLOWE which computes trajectories of test particles striking a wall and scattering off the atoms in the crystalline lattice of the wall, ultimately coming to rest in the wall or escaping with a reduced velocity. For each species of incident test flux, assuming in our case a smooth amorphous wall of iron, a scattering distribution is computed which is a five-dimensional differential distribution $P(v, \theta, \phi, E, \alpha)\, v^2\, dv \sin\theta\, d\theta\, d\phi$, in terms of incident energy $E_{\text{in}}$, incident polar angle $\alpha$, and outgoing speed $v$, polar angle $\theta$, and azimuthal angle $\phi$ relative to the plane of the incident test flux and wall normal (Fig. 3). The fraction of incident particles reflected as a function of incident $E$ and $\alpha$ is also computed.

Given incident $E_{\text{in}}$ and $\alpha$, the three-dimensional distribution

$$P_{E,\alpha}(v, \theta, \phi)\, v^2\, dv \sin\theta\, d\theta\, d\phi$$

must be sampled. Now $Pv^2\, dv \sin\theta\, d\theta\, d\phi$ will be highly peaked at points, both for physical reasons and because of too few Monte-Carlo scorings for a smooth result. Thus care must be taken in designing a fast sampling algorithm which is economical in storage.

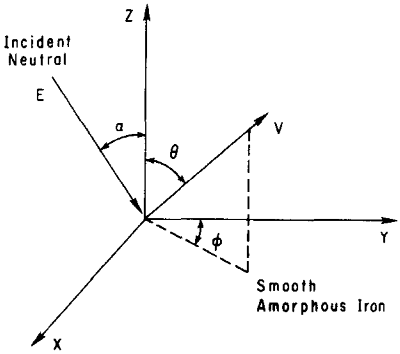

FIG. 3. Coordinate system for MARLOWE wall reflection data.

In our algorithm we first reduce the sampling of $Pv^2\,dv\sin\theta\,d\theta\,d\phi$ to sampling consecutively from the three one-dimensional distributions $f^1, f^2$, and $f^3$, defined by

$$f^1_{E,\alpha}(v) = \iint P_{E,\alpha}(v,\theta,\phi)\sin\theta\,d\theta\,d\phi,$$

$$f^2_{E,\alpha}(\theta) = \int P_{E,\alpha}(v_0,\theta,\phi)\,d\phi,$$

and

$$f^3_{E,\alpha}(\phi) = P_{E,\alpha}(v_0,\theta_0,\phi).$$

These distributions are stored as follows. Each distribution is given by $n$ data points $x_1 \leqslant x_2 \leqslant \cdots \leqslant x_n$. For $0 < \xi \leqslant 1$, if $(i/n) \leqslant \xi < [(i+1)/n]$ set $x_\xi = x_i$. Then we store $x_\xi$, for $\xi = 0.1$, 0.3, 0.5, 0.7, and 0.9, for each distribution of $f^1, f^2$, and $f^3$ forming the arrays $F^1_{E,\alpha}(\xi)$, $F^2_{E,\alpha}(\eta,\xi)$, and $F^3_{E,\alpha}(\zeta,\eta,\xi)$, using $\alpha = 0$, 20, 40, 60, 80°, and $E = 50$, 100, 200, 500, and 1000 eV. Thus, the largest array needed, $F^3_{E,\alpha}$, has size $5^5 = 3125$.

For example, Table II gives $F^1$, $F^2$, and $F^3$, for $E_{\text{in}} = 200$ eV, $\alpha = 0°$. The reflection coefficient is 0.4320. If a reflection occurs, three choices of a uniform random variable on the unit interval are made, say $\xi = 0.3$, $\eta = 0.5$, and $\zeta = 0.9$. Then $v = F^1(2) = 100$ eV, $\cos\theta = F^2(3,2) = 0.6497$, and $\cos\phi = F^3(5,3,2) = -0.5448$ (it is more convenient to store $\cos\theta$ and $\cos\phi$ than $\theta$ and $\phi$). For more general $\xi$, $\eta$, and $\zeta$, we derive $v$, $\cos\theta$, and $\cos\phi$ through linear interpolation of $F^1$, $F^2$, and $F^3$.

A comparison of these two models will be found in [8]. Typically we use the MARLOWE model for $50\text{ eV} \leqslant E_{\text{in}} \leqslant 1000\text{ eV}$, and the first model for $E_{\text{in}}$ outside that range. This is because assumptions in MARLOWE may not be valid for $E_{\text{in}} < 50$ eV, and computing the arrays $F^1$, $F^2$, and $F^3$ for $E_{\text{in}} > 1000$ eV is very expensive.

Wall sputtering rates for various materials were fitted from the data of Roth *et al.* [9]. The angular dependence of the rate was assumed to be proportional to $[\cos(\text{polar angle})]^{(-1.5)}$.

## III. THE MONTE-CARLO ALGORITHM

In our time-independent calculation a profile consists of a set of test flights (Fig. 4). This section describes how these flights are initiated, flown, and integrated to yield the physical parameters of interest.

### A. *Test-Flight Initialization*

The source of neutrals comes from ions flowing into the neutralizer plate. Given a one-dimensional ion-current distribution hitting the plate from a separate computation, initial positions $P_0$ at the wall are selected. Each test flight represents

TABLE II[a]

| $E = F^1(\xi)$(eV) | | | | |
|---|---|---|---|---|
| 57.3 | 100. | 127.5 | 150.8 | 168.5 |
| $\cos\theta = F^2(\eta,\xi)$ | | | | |
| 0.5104 | 0.6931 | 0.8096 | 0.8926 | 0.9672 |
| 0.4843 | 0.6817 | 0.8009 | 0.8869 | 0.9654 |
| 0.4753 | 0.6497 | 0.7727 | 0.8681 | 0.9609 |
| 0.4646 | 0.6475 | 0.7642 | 0.8642 | 0.9522 |
| 0.3343 | 0.5088 | 0.6313 | 0.7533 | 0.8867 |
| $\cos\phi = F^3(\zeta,\eta,\xi)$ | | | | |
| $F^3(1,\eta,\xi)$ | | | | |
| -0.9460 | -0.5096 | -0.0494 | 0.5299 | 0.9293 |
| -0.9224 | -0.5758 | 0.0270 | 0.5498 | 0.9519 |
| -0.9481 | -0.6291 | 0.0147 | 0.5343 | 0.9507 |
| -0.9501 | -0.5564 | 0.0380 | 0.5548 | 0.9442 |
| -0.9594 | -0.5536 | 0.1303 | 0.6682 | 0.9567 |
| $F^3(2,\eta,\xi)$ | | | | |
| -0.9510 | -0.6303 | -0.1349 | 0.5591 | 0.9501 |
| -0.9448 | -0.6107 | -0.0077 | 0.4643 | 0.9378 |
| -0.9362 | -0.4654 | 0.0031 | 0.5703 | 0.9513 |
| -0.9322 | -0.5519 | -0.0030 | 0.5741 | 0.9734 |
| -0.9388 | -0.5297 | 0.1150 | 0.5879 | 0.9400 |
| $F^3(3,\eta,\xi)$ | | | | |
| -0.9308 | -0.5249 | 0.1161 | 0.6025 | 0.9511 |
| -0.9346 | -0.6454 | -0.0176 | 0.4700 | 0.9325 |
| -0.9448 | -0.5862 | -0.0408 | 0.6021 | 0.9694 |
| -0.9341 | -0.5364 | -0.0625 | 0.5133 | 0.9494 |
| -0.9474 | -0.5254 | -0.0254 | 0.5714 | 0.9646 |
| $F^3(4,\eta,\xi)$ | | | | |
| -0.9095 | -0.5492 | 0.0054 | 0.5960 | 0.9142 |
| -0.9395 | -0.6243 | -0.0676 | 0.6596 | 0.9630 |
| -0.9670 | -0.5826 | -0.0809 | 0.5839 | 0.9256 |
| -0.9401 | -0.5702 | 0.0194 | 0.5559 | 0.9450 |
| -0.9376 | -0.4852 | 0.0458 | 0.6537 | 0.9589 |
| $F^3(5,\eta,\xi)$ | | | | |
| -0.9343 | -0.6085 | -0.0343 | 0.5889 | 0.9491 |
| -0.9199 | -0.5429 | 0.0072 | 0.6042 | 0.9324 |
| -0.9343 | -0.5448 | 0.0822 | 0.6140 | 0.9716 |
| -0.9217 | -0.4109 | 0.1232 | 0.6503 | 0.9696 |
| -0.9243 | -0.4775 | 0.0642 | 0.6172 | 0.9532 |

[a] Results from MARLOWE code for incident energy $E = 200$ eV, polar angle of $\alpha = 0°$. The fraction of incident particles reflected is 0.4320.

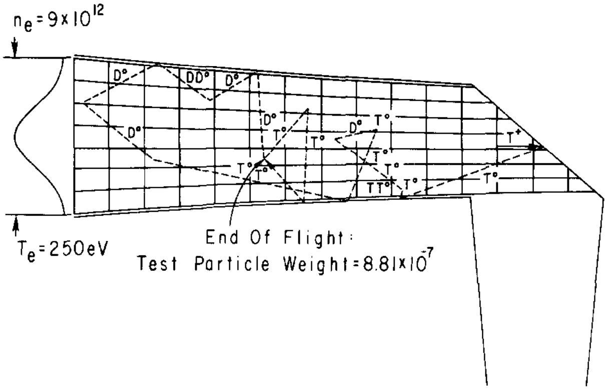

FIG. 4. Sample test flux flight. A triton ion strikes the neutralizer plate, reflects as a $T^0$ atom, strikes a wall, desorbs as a $TT^0$ molecule, dissociates, undergoes a further sequence of plasma/wall collisions until its weight is less than a set minimum (here $10^{-6}$), where a pure ionization occurs ending the flight. Plasma is 5% $He^{2+}$, 47.5% $D^+$, 47.5% $T^+$.

$\omega_0 = Q_{\text{wall}}/N$ real particles per second, where $Q_{\text{wall}}$ is the total current on the walls, and $N$ is the total number of test flights. Initial velocity $v$ is determined by assuming that the initial ion energy is increased at the plate by a selected sheath potential and then attenuated by striking normal to the wall and reflecting or sticking.

### B. *Test-Flight Tracking*

Given the initial position $P_0$, velocity $v$, and atomic species, we are ready to begin the test flight. We use the pseudocollision algorithm, based on the idea of pseudocollisions in [10]. Our version is flow charted in Fig. 5.

At the beginning of each profile, two two-dimensional arrays $R_1(i,j)$ and $R_2(i,j)$ containing plasma zone indices in a finer uniform rectangular grid are constructed (Fig. 6). Given a position $P$ in the device, its coordinates $(i_P, j_P)$ in the reference meshes are easily computed, and its plasma zone coordinates $I = R_1(i_P, j_P)$, $J = R_2(i_P, j_P)$ looked up, determining the plasma conditions at $P$.

The pseudocollisional algorithm uses this information as follows. Choosing the number of mean free paths $\mu = -\ln \xi$, $\xi$ a uniform random variable, $0 < \xi \leqslant 1$, the position of the test flight is moved a distance $\mu\lambda_{\text{min}}$, where $\lambda_{\text{min}}$ the shortest mean free path length in the entire given plasma for a test flight with the velocity $v$. Assuming a wall has not been hit, the local mean free path length at the new position, $\lambda_{\text{local}}$, is computed using the reference arrays. The ratio $\rho = \lambda_{\text{min}}/\lambda_{\text{local}}$ represents the probability that a real collision occurs at the new point. If a test does not result in a collision, we say a pseudocollision has occurred, and we repeat the process choosing a new $\mu$, moving a distance $\mu\lambda_{\text{min}}$ and so on until the test flight hits a wall, leaves the device, or finally does undergo a plasma collision.

Our pseudocollisional algorithm may be compared to the path-length estimator of [11]. A poof of their equivalence is given in [12]. A disadvantage of the path-length

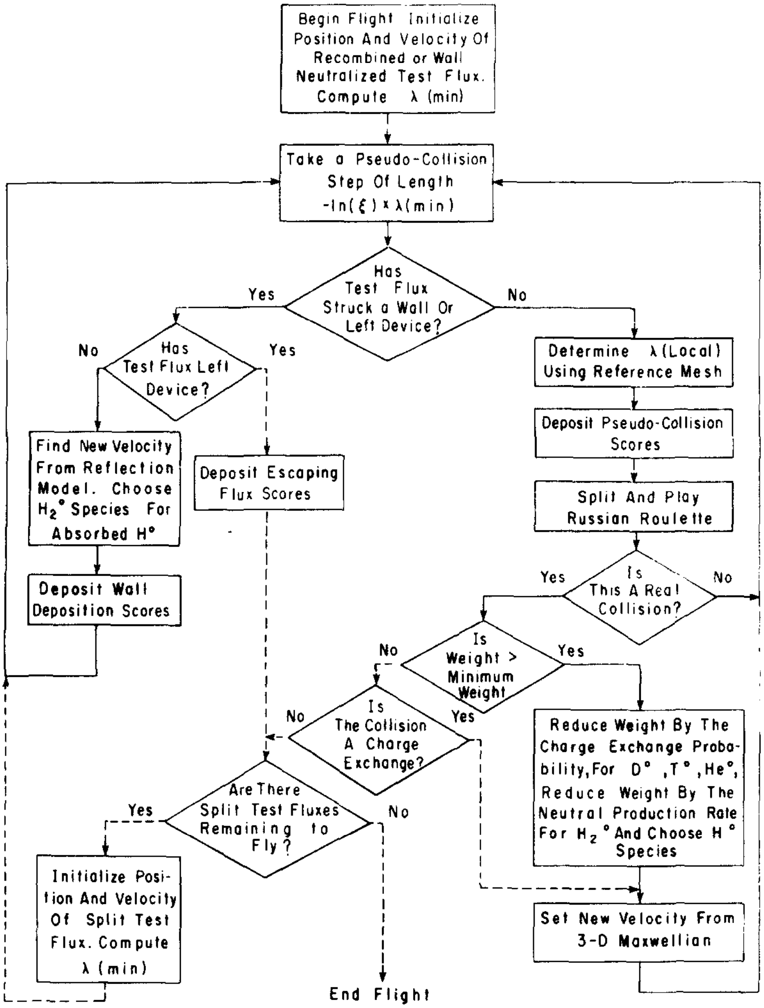

FIG. 5. Flowchart of the pseudocollision algorithm.

estimator method is the time-consuming geometric calculations required in computing the points of intersection of flight paths with zone boundaries. An advantage of the pseudocollisional algorithm over the path-length estimator algorithm is, then, that the reference arrays $R_1, R_2$ contain the only detailed geometric calculation necessary. Thus the amount of geometric calculation is independent of the number of test flights flown. The algorithm described above to compute them is quite efficient, computing 300 × 300 reference arrays in less than 1 CPU sec on the CRAY-1 and packing the arrays so as to reduce storage.

A disadvantage of the pseudocollisional algorithm is that $\lambda_{\min}$ must be computed very often. We thus make a table of $\lambda_{\min}$ at the start of a set of profiles as a function

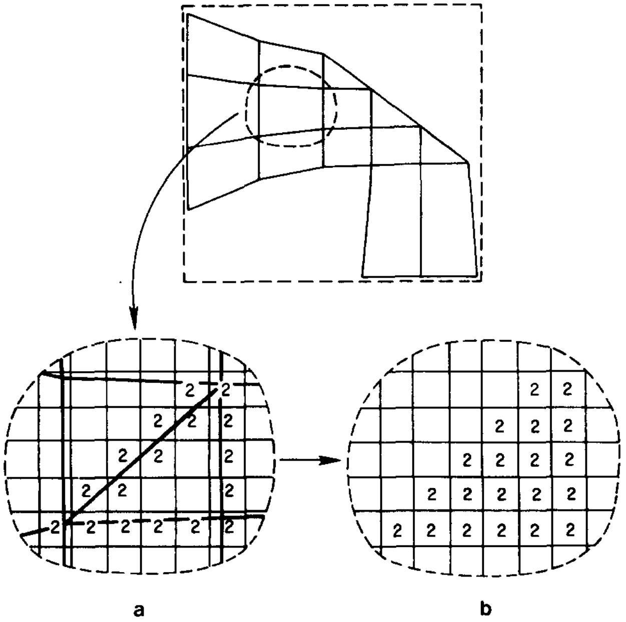

FIG. 6. Construction of the zone reference array for the pseudocollision algorithm. (a) Triangle edges are traced onto reference array using plasma zone index of the triangle. (b) Traced triangle is filled in.

of neutral velocity, species, plasma density, and temperature. Note that since the algorithm requires only that the step size be no longer than $\lambda_{\min}$, smaller lengths, derived from worst case study of $n\langle\sigma v\rangle$ rates, can remove the need for the large $\lambda_{\min}$ table. However, underestimating $\lambda_{\min}$ means more test steps to a collision, reducing efficiency, so care must be used in choosing $\lambda_{\min}$ if this method is used.

### C. *Test-Flight Weighting*

We use the method of suppressed absorption, as in [11]: at each collision, the charge exchanging probability

$$P_{cx} = \lambda_{cx}/\lambda_{\text{local}}$$

is computed, where $\lambda_{cx}$ is the local mean free path length due to charge exchange only. The test flight is then "split" between ionization and charge exchange by reducing its weight $\omega$ to $P_{cx}\omega$ to account for attenuation by ionization. Thus a weight of $\omega_{\text{ion}} = (1 - P_{cx})\omega$ is ionized.

If, however, $\omega$ falls below a given minimum, this "splitting" is stopped, and a choice is made between a pure charge exchange, continuing the flight with $\omega$ unchanged, or pure ionization, setting $\omega = 0$, and ending the flight.

After modifying $\omega$ in the suppressed absorption algorithm, to conserve energy, $\omega$ is further scaled by a factor $\kappa = \sigma_{cx}\,|v|/\langle\sigma_{cx} v\rangle$ to account for the charge-exchange cross sections being nonconstant over the Maxwellian distribution of ions. Here $\sigma_{cx}$ is the charge-exchange cross section. We do not at present include any angular dependence in our charge-exchange model.

### D. *Integration Methods*

The pseudocollision algorithm computes ionization and charge-exchange rates directly. For example, the sum over all collisions in a zone, $S_{\text{ion}} = \sum \omega_{\text{ion}}$, gives the total test-flight weight ionized in that zone. Multiplying by the total number of test flights $N$ gives the ionization rate in ionizations per second. Similar sums are made representing charge exchange rates, ionization, and charge exchange energies, exiting currents, power deposition, and erosion rates at the walls. The neutral density $n_0$ is derived from

$$NS_{\text{ion}}/V = n_e n_0 \langle\sigma_{ei} v\rangle, \tag{3.1}$$

where $V$ is the zone volume, $n_e$ the local electron density, and $\sigma_{ei}$ the electron ionization cross section. The average energy $\tilde{E}$ of a neutral being ionized is

$$\tilde{E} = W_{\text{ion}}/S_{\text{ion}}, \qquad \text{where} \quad W_{\text{ion}} = \sum \omega_{\text{ion}} E, \tag{3.2}$$

the sum again being over all collisions, with $E$ the energy of the ionized neutral.

One weakness of this scoring method is that scoring events occur only at collisions. To score at each pseudocollision we modify the scoring method above by taking for $S_{\text{ion}}$, for example, the sum

$$S'_{\text{ion}} = \sum \rho\omega_{\text{ion}}$$

over all pseudocollisions, where $\omega_{\text{ion}}$ is as above, and $\rho = \lambda_{\text{min}}/\lambda_{\text{local}}$ is the real collision probability. On the average, $S'_{\text{ion}} = S_{\text{ion}}$, but the variance in $S'_{\text{ion}}$ is less than that of $S_{\text{ion}}$, for now a collision requiring $n$ pseudocollisions deposits $n$ scores instead of 1.

Another weakness is that in regions containing no plasma, our sums are zero since $\lambda_{\text{local}}$ is infinite. To compute the neutral density here, we assume a "pseudoplasma" present, consisting of pseudoions whose reaction with an atom leaves the atom unchanged in every aspect. We assume the local reaction rate of this ficticious reaction to be a preselected fraction of the average total (real) plasma reaction rates, to achieve comparable variances. Neutral density and temperature can then be computed as in (3.1) and (3.2), with the electron ionization quantities replaced by the appropriate pseudoion quantities.

### E. *Variance Reduction Techniques*

Most collisions occur near the plate, resulting in a wealth of scorings there, compared to very few in regions far away. To improve the variance in these distant regions, we use a standard splitting/Russian roulette algorithm [13]. Using larger zones in regions far from the plate also increases the number of scorings per zone away from the plate while keeping greater resolution near the plate, where it is needed due to the larger gradients in the ionization/charge exchange rates there. Suppression of absorption, described above, increases the number of scorings in the more distant zones by keeping test fluxes alive which otherwise would be killed off by ionization. Finally, our technique of scoring at each pseudocollision is an improvement over recording the scores only at collisions.

### F. *Optimization and Performance*

Improvements in efficiency at the programing level by factors of 2 to 3 on a vectorizing machine, such as the CRAY-1, can come from modularizing the particle-tracking algorithm shown in Fig. 5 and performing each segment in loops over 64 or 128 test fluxes. The arrays containing test-flux data are merged at each step, discarding the test flights as they finish their flights. We have found that the added overhead cost of merging is small compared to savings gained from vectorization. The mergers are not easily vectorized, but they consist mostly of assignment statements, while the expensive calculations in particle tracking are now done in vectorized loops.

Performance on the CRAY-1 requires 8–10 CPU sec/1000 test flights for a typical INTOR calculation, with 500 to 2000 test flights used for a typical profile. The program consists of ~4000 of Fortran IV executable statements and uses ~40,000 decimal words of array storage.

## IV. EXAMPLE CALCULATIONS

We include two applications of our algorithm, molecular flow through rectangular tubes for comparison with analytical analysis, and calculations of performances of proposed INTOR divertors, which exercise many of the subcalculations described in Section III.

### A. *The Vacuum Case*

We model the case of molecular flow through a tube of rectangular cross section with width $b \gg$ than height $a$ and length $l$. Clausing [14] has deduced values for $K = Q_f/Q_{in}$, where $Q_{in}$ is the incoming current and $Q_f$ the current exiting the far outlet. Table III lists his values, $K_{Cl}$, of $K$ along with the values, $K_{MC}$, of $K$ computed by us, for $l/a$ varying from 0.2 to 10.0, using $10^6$ test flights and assuming a cosine distribution in the polar angle to the wall of velocities of reflecting particles. For $0.1 < l/a < 4.0$, $|K_{Cl} - K_{MC}| < 3\sigma_M$, and for $5.0 \leqslant l/a \leqslant 10.0$ we still have good agreement with $|K_{Cl} - K_{MC}|/K_{Cl} \leqslant 2.0\%$.

### B. *Proposed INTOR Divertors*

The effects of the plasma on helium and hydrogen pumping, plasma source rates, heat loads on the divertor walls and neutralizer plates, and the erosion rates for the

TABLE III[a]

| $l/a$ | $K_{\mathrm{Cl}}$ | $K_{\mathrm{MC}}$ | $\sigma_M$ |
|---|---|---|---|
| 0.1 | 0.9525 | 0.9527 | 0.0002 |
| 0.2 | 0.9096 | 0.9099 | 0.0003 |
| 0.4 | 0.8362 | 0.8360 | 0.0004 |
| 0.8 | 0.7266 | 0.7262 | 0.0004 |
| 1.0 | 0.6848 | 0.6847 | 0.0005 |
| 1.5 | 0.6024 | 0.6023 | 0.0005 |
| 2.0 | 0.5417 | 0.5423 | 0.0005 |
| 3.0 | 0.4570 | 0.4575 | 0.0005 |
| 4.0 | 0.3999 | 0.3984 | 0.0005 |
| 5.0 | 0.3582 | 0.3565 | 0.0005 |
| 10.0 | 0.2457 | 0.2411 | 0.0004 |

[a] Ratios $Q_f/Q_{\mathrm{in}}$ of the molecular current $Q_f$ leaving the far end of a tube of rectangular cross section $a \times b$ and length $l$, $b \gg a$, $b \gg l$, to the current entering, $Q_{\mathrm{in}}$, as computed by our algorithm ($K_{\mathrm{MC}}$) and by Clausing ($K_{\mathrm{Cl}}$) [13], for $l/a = 0.1$ to 10.0. The standard deviation $\sigma_M$ in the calculation of $K_{\mathrm{MC}}$ is $[K_{\mathrm{MC}}(1-K_{\mathrm{MC}})/M]^{1/2}$, where $M = 10^6$ test flights.

neutralizer plate and divertor walls were computed for a variety of INTOR model poloidal divertors and diverted plasmas.

A pumping calculation was made for a geometry similar to that shown in Fig. 1b, but with a rectangular instead of hyperbolic throat. Cases were studied with the density having a Gaussian profile of $8.8 \times 10^{12}\ \mathrm{cm}^{-3}$ at the center falling to $1.1 \times 10^{12}\ \mathrm{cm}^{-3}$ at the channel walls, and central temperature of 250 eV, varying with the same Gaussian profile as the density. The pumping speed of the pump is approximated by that of a thin slot [14]

$$3.638 K_{\mathrm{Cl}}\, ab(T/M)^{1/2} \quad \text{liters/sec,} \tag{4.1}$$

TABLE IV

Relative Pumping Rates for D, T, and He in Rectangular Divertors[a]

| Case | $l$ (cm) | $a$ (cm) | $R = Q_p/Q_t$ D | $R = Q_p/Q_t$ T | $R = Q_p/Q_t$ He | $E$ | $R_{\mathrm{vac}}$ | $C = R/R_{\mathrm{vac}}$ DT | $C = R/R_{\mathrm{vac}}$ He |
|---|---|---|---|---|---|---|---|---|---|
| 1 | 80 | 30 | 2.67 | 3.83 | 0.56 | 5.80 | 0.20 | 16.3 | 2.8 |
| 2 | 50 | 30 | 0.53 | 0.70 | 0.25 | 2.46 | 0.16 | 3.9 | 1.6 |
| 3 | 50 | 40 | 0.26 | 0.39 | 0.13 | 2.50 | 0.11 | 3.0 | 1.2 |
| 4 | 100 | 30 | 1.94 | 2.20 | 1.23 | 1.68 | | | |

[a] Divertor throats are $l \times a$ cm, and pumps are $40 \times 8$ cm. $Q_p$ and $Q_t$ are the currents leaving the pump and throat, respectively. $E$ is the ratio of $R = Q_p/Q_t$ for DT over $R$ for He. $R_{\mathrm{vac}}$ is the ratio of pump to throat conductances computed for a vacuum using (4.1), and $C$ is $R$ over $R_{\mathrm{vac}}$.

where $K_{\mathrm{Cl}}$ is the Clausing factor in Table III, $T$ is in degrees Kelvin, $M = 5$ is the atomic weight of DT, the pump length $l$ is 40 cm, and the width $b$ is 25 cm. Assuming 12 such pumps in the device, a pump width of $a = 8$ cm provides 24,200 liters/sec of pumping for the whole torus.

The relative pumping speeds with the plasma of three such cases varying the throat dimensions are listed in Table IV. The ratio $R = Q_p/Q_t$, the current $Q_p$ of neutral particles exciting through the pump divided by the current $Q_t$ returning to the main plasma, is given for D, T, and He. $R_{\mathrm{vac}}$ is the ratio of the geometric pumping speed of the pump to that of the return channel to the main plasma, given by (4.1).

The ratios of the Monte-Carlo calculations of the various $R$'s to the geometric $R_{\mathrm{vac}}$ reflect the effect of the plasma reducing the neutral backflow from the neutralizer plate to the main plasma and in raising the effective pumping speed of the pump. The ratios in Table IV, cases 1–3, vary from 16.3 for the $80 \times 30$ hydrogen case to 1.2 for the $50 \times 40$ helium case.

We note that these three cases scale in a reasonable way. As we make the channel shorter, or wider, relatively more particles return to the main plasma. Applying (4.1) to the $80 \times 30$ and $50 \times 30$ cases, the ratio $R$ should reduce by a factor of 0.81 as the channel length is decreased. The actual reduction is about 0.19 for hydrogen and 0.44 for helium, indicating that the plasma appreciably retards the neutral backflow to the main plasma. Since lengthening the channel increases the ionization and charge exchange "optical depth" of the divertor channel, it is not surprising that the geometric scaling underestimates the effect.

Since widening the channel for a given length does not increase the optical depth of the channel, however, one would expect in this case that the geometric scaling in (4.1) will be closer to the divertor result. It predicts a reduction in the $R$ by a factor of 0.69 from the $50 \times 30$ case compared to the $50 \times 40$ case. This is fairly close to the Monte-Carlo results (0.49 for D, 0.56 for T, and 0.52 for He), indicating that one can use the geometric scaling for estimating the effects of varying the channel width.

In order to compare our algorithm with an independent one, we computed Table IV, case 4, also treated by Seki *et al.* [4]. It assumes a rectangular channel 100 cm long and 30 cm wide with a 20-cm-wide plasma (47.5% $D^+$, 47.5% $T^+$, and 5% $He^{2+}$), of uniform electron density of $3 \times 10^{12}$ cm$^{-3}$, and temperature of 250 eV. Their pump model, reflecting a fixed fraction entering the pump opening instead of tracking test fluxes in the pump, and their neutral reflection data, were used also by us. Our more detailed treatment of molecules was retained.

The backflow $B = Q_t/(Q_p + Q_t) = 1/(1 + R)$ in their calculation varied from 0.7 to 0.46 for DT, and from 0.7 to 0.23 for He as the density varied from $8 \times 10^{12}$ to $10^{12}$ cm$^{-3}$. Thus their helium enrichment varies from 1 to 2. In particular, their result for a density of $3 \times 10^{12}$ cm$^{-3}$ has an enrichment of $B_{\mathrm{He}}/B_{\mathrm{H}} = 1.13$. Our case at that density yields backflows of 0.34 for D, 0.31 for T, and 0.44 for He. This gives us a helium deenrichment of $B_{\mathrm{He}}/B_{\mathrm{H}} = 0.75$. Considering the uncertainties in the wall-reflection models, the different atomic physics, and differences in the code, this discrepancy probably is not significant.

A set of calculations of plasma-source rates and wall-erosion rates was carried out

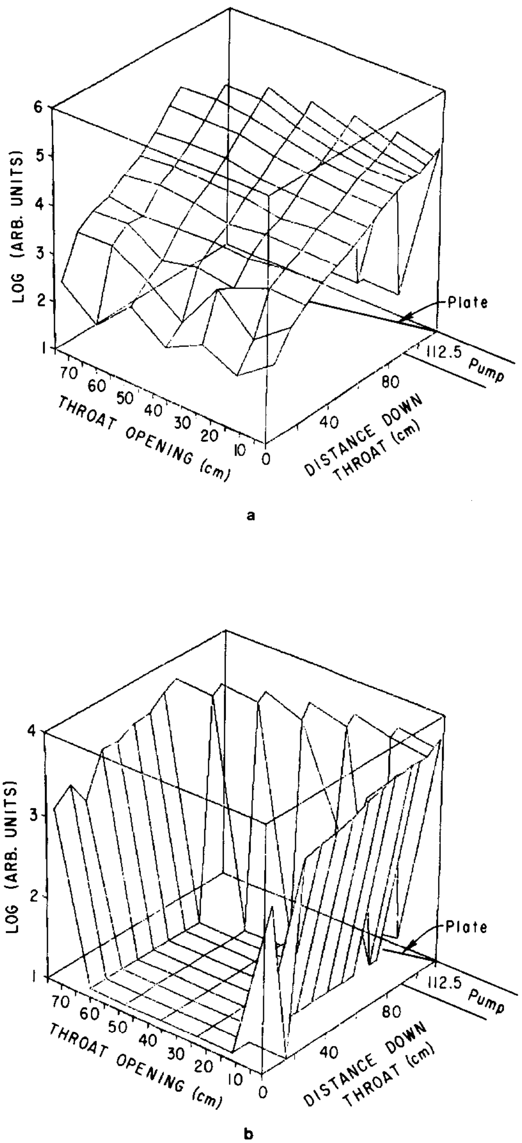

FIG. 7. Ionization rate profile for (a) $D^+$ and (b) $D_2^+$ production in sample 70 × 112.5-cm INTOR divertor.

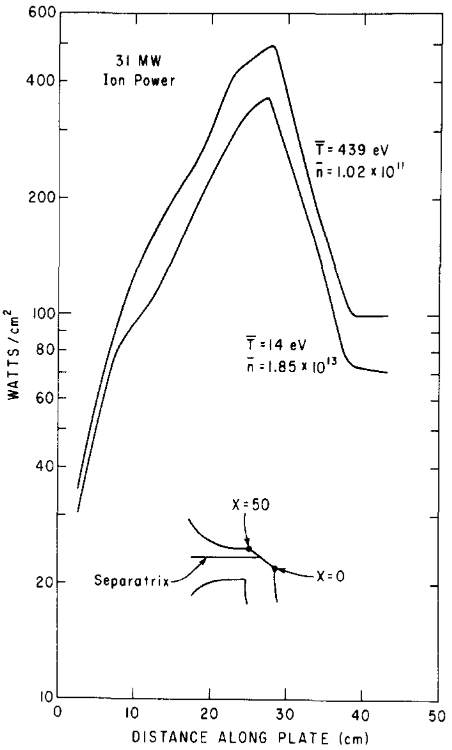

FIG. 8a. Power loads at the neutralizing plate for the INTOR divertor.

for a more realistic hyperbolic geometry (Fig. 2a), but with throat width of 70 cm instead of 60 cm. Typically, the hydrogen ionization sources are peaked at the neutralizer plate (Fig. 7a) falling gradually toward the divertor throat, and the molecules are ionized at the edge of the plasma (Fig. 7b). Neutral impurities, such as iron, are produced by sputtering at the neutralizer plate and walls. Since the neutral impurity atoms are low energy (~3 eV) and heavy ($A = 57$), their mean free path for first ionization is short, and they are ionized within 2 cm of the neutralizer plate.

The energy deposited on the walls and neutralizer plates was computed for a variety of sample plasmas with temperatures varying from 14 to 439 eV, and with the density scaled appropriately from $1.85 \times 10^{13}$ to $10^{11}$ cm$^{-3}$ to maintain constant energy flux. The power on the neutralizer plate did not vary greatly (Fig. 8a). It peaks at the separatrix at ~400 W cm$^{-2}$ and falls off rapidly. The erosion rates of the divertor plates and walls were calculated also for a 500-eV $10^{12}$-cm$^{-3}$ diverted plasma. The erosion rate of the iron plate peaks at 26 cm/year at the separatrix for a 100% duty cycle (Fig. 8b). The erosion rates of the divertor walls are much lower, falling rapidly with distance from the neutralizer plate (Fig. 8c).

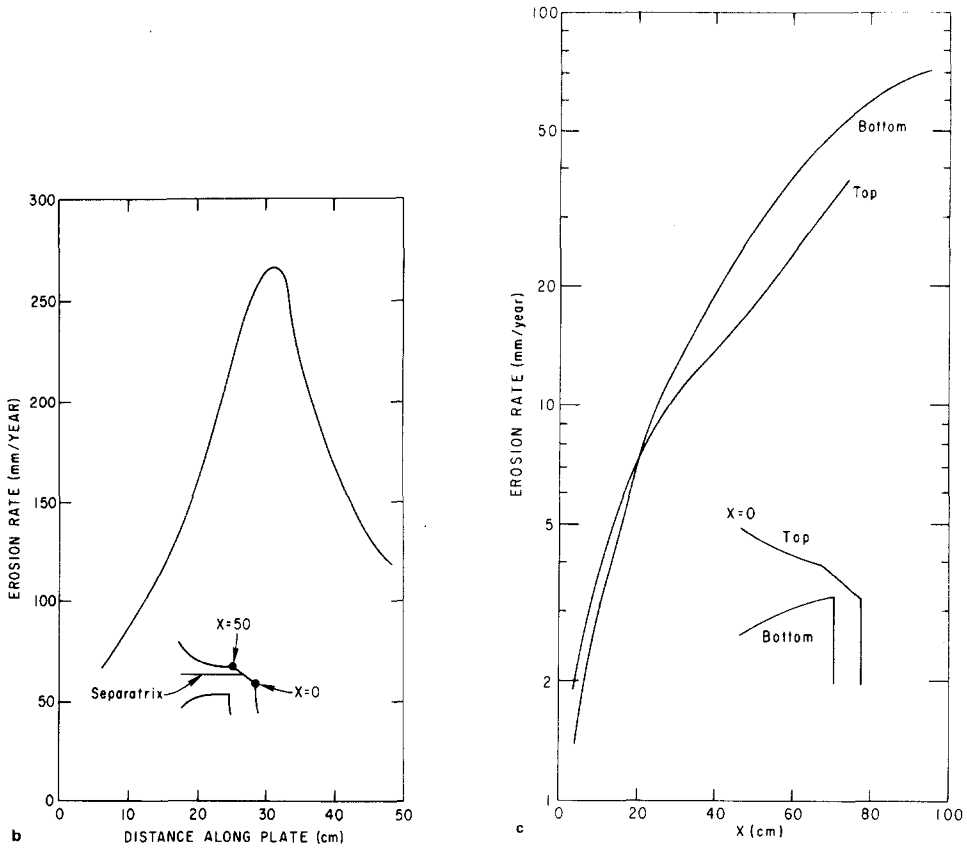

FIGS. 8b, c. Erosion rates of (b) iron neutralizing plate and (c) divertor walls for a 500 eV, $10^{2}\,\mathrm{cm}^{-3}$ diverted plasma (100% duty cycle).

## ACKNOWLEDGMENTS

The authors thank Dr. Paul Rutherford, Dr. John Schmidt, Dr. Francis Perkins, and Dr. Allen Boozer for encouragement and useful discussions. They also thank Dr. Mark Robinson for the use of MARLOWE and his assistance in using it.

This work was supported by the U.S. Department of Energy Contract DE-AC02-76-CHO-3073.

## REFERENCES

1. International Tokamak Reactor, Zero Phase, IAEA, Vienna, Austria, 1980.
2. M. T. ROBINSON *et al.*, *Phys. Rev. B* 9 (1974), 5008.
3. J. CALLEN *et al.*, IAEA-CN-38/Y-3, 8th Intern. Conf. on Plasma Physics and Controlled Nuclear Fusion Research, IAEA, Vienna, 1981.

4. Y. SEKI *et al.*, *Nucl. Fusion* **20** (1980), 10.
5. M. PETRAVIC *et al.*, *Phys. Rev. Lett.* **48** (1982), 326.
6. R. L. FREEMAN AND E. M. JONES, CLM-R 137, Culham Lab., Abingdon, Perkshire, England, 1974.
7. E. M. JONES, CLM-R 175, Culham Lab., Abingdon, Berkshire, England, 1977.
8. G. BATEMAN, "Distribution of Neutrals Scattered Off a Wall," PPPL Appl. Phys. Rep. 1, Princeton, New Jersey, 1979.
9. J. ROTH, J. BOHDANSKY, AND W. OTTENBERGER, IPP-9/26, Max-Planck-Institut für Plasmaphysik, 1979.
10. A. S. KUKUSHKIN, V. I. PISTUNOVICH, AND S. V. PUTVINSKI, IAEA-CN-35/B4, Plasma Physics and Controlled Nuclear Fusion Research, IAEA, Vienna, Austria, 1977.
11. M. HUGHES AND D. POST, *J. Comput. Phys.* **28** (1978), 43.
12. G. G. LISTER, D. E. POST, AND R. J. GOLDSTON, "Proceedings, 3rd Symp. on Plasma Heating in Toroidal Devices," pp. 303–307, Ed. Compositori, Bologna, 1976.
13. J. M. HAMMERSLEY AND D. C. HANDSCOMB, "Monte-Carlo Methods," Metuchen, London, 1964.
14. P. CLAUSING, *Ann. Physik* **12** (1932), 961.